Advances in Water Resources 184 (2024) 104622

Contents lists available at ScienceDirect

Advances in Water Resources

journal homepage: www.elsevier.com/locate/advwatres

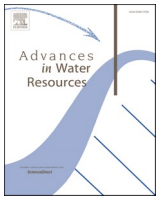

# Bifurcating paths: The relation between preferential pathways, channel splitting, under sampled regions, and tortuosity on the Darcy scale

Avioz Dagan, Yaniv Edery *

*Faculty of Civil and Environmental Engineering, Technion, Haifa, Israel*

ARTICLE INFO

*Keywords:*
Transport
Porous media
Bifurcations
Tortuosity
Fractal dimension
Darcy-scale

ABSTRACT

Transport in porous media on the Darcy scale can be both Fickian and non-Fickian, an outcome dependent on the degree of homogeneity of the hydraulic conductivity pattern, as well as the boundary conditions and flow rate. The non-Fickian manifestation is generally associated with heterogeneous media, which promotes the formation of preferential pathways that funnel the transport. Yet this funneling occurs in both weakly and strongly heterogeneous domains, through a mechanism that is yet to be fully characterized. We model Darcy-scale transport using a particle tracking code (PT) that samples a 2D, lognormally distributed conductivity field with a variance representing a range of homogeneous to heterogeneous domains. We find that the resulting preferential pathways tend to split into more pathways (bifurcations), leaving regions into which particles do not invade, which we refer to as "under sampled regions" (USR), while forming a tortuous path. The fraction of bifurcations decreases downstream, reaching an asymptotic value, with a trend that can be fitted as a power-law of the variance. We show that the same power-law exponent relating the bifurcations to the variance holds true for the USR fraction, tortuosity, and fractal dimension with the same variance. An extension of our work is also presented for varying correlation length of the conductivity spatial distribution. We further expand our analysis to a case of impermeable fraction in a uniform conductivity field and show that the power-law fit still holds.

**Key Points**

Preferential pathways at the Darcy scale can be characterized by their bifurcations, and USR formation formed by their tortuous path.

The bifurcation fraction, USR, tortuosity, and fractal dimension scale with the conductivity heterogeneity.

The same power law exponent captures the scaling of bifurcation fraction, USR, tortuosity, and fractal dimension.

## 1. Introduction

Transport in saturated porous media is of vast relevance to many disciplines, including chemical transport in soils, aquifers and fractured rocks (Bear, 2013; Edery et al., 2016a; Haggerty et al., 2001; Raveh-Rubin et al., 2015), oil recovery (Edery et al., 2018; Lenormand et al., 1983), filtration (Tufenkji and Elimelech, 2004), fuel cells (Pharoah et al., 2006), and even coffee percolation (Fasano and Talamucci, 2000). However, the medium in a natural, porous environment typically forms a heterogeneous structure, where the transport is often non-Fickian, featuring heavy tails in the tracer concentration distribution that can be captured by various models (Berkowitz and Scher, 1997; Cirpka and Kitanidis, 2000; Cushman and Ginn, 1993; Dullien, 2012; Haggerty et al., 2000; Kang et al., 2011; Le Borgne et al., 2008; Morales-Casique et al., 2006a; 2006b; Sánchez-Vila and Carrera, 2004; Willmann et al., 2008). Such transport through a heterogeneous porous medium can be regarded as transport within often described as transport through lognormally distributed conductivity bins in space (Gómez-Hernández and Journel, 1993), and the variance of the lognormal distribution marks the field heterogeneity (Sanchez-Vila et al., 2006). The local flow within each area forming this heterogeneous field can be locally solved by the Darcy law, while the transport is described by the Darcy velocity and the diffusion using the Langevin equation, which gives rise to non-Fickian transport on the larger continuum scale, among other processes that lead to anomalous transport (Edery, 2021; Edery et al., 2014).

A persistent outcome of the heterogeneity, both experimentally and numerically, is the advent of preferential pathways, defined as the non-

* Corresponding author.
*E-mail address:* yanivedery@technion.ac.il (Y. Edery).

https://doi.org/10.1016/j.advwatres.2024.104622
Received 20 June 2023; Received in revised form 9 January 2024; Accepted 9 January 2024
Available online 10 January 2024

uniform spatial concentration of a tracer as it migrates through the porous medium (Cirpka and Kitanidis, 2000; Willmann et al., 2008), forming tortuous paths for the tracer trajectories (Comolli and Dentz, 2017; Comolli et al., 2019; Hakoun et al., 2019). In these paths, the tracer is directed, or funneled, into narrower flow paths with the lowest resistance to flow; this leads to increasing formation of under sampled regions (USR) in regions with resistance higher than average, where the tracer bypasses or visits in quantities that are orders of magnitude smaller than the average concentration (Webb and Anderson, 1996). This relation between preferential pathways and hydraulic conductivity distribution is observed at the Darcy scale (Bianchi et al., 2011; Edery et al., 2016a; Riva et al., 2010, (2008), numerically (Fiori and Jankovic, 2012), and at the pore scale (Bijeljic et al., 2013; Kang et al., 2014; Zhang and Lv, 2007).

These preferential pathways were linked directly to connectivity and early arrival times measured by the breakthrough curve, and the hydraulic resistance through graph theory (Rizzo and de Barros, 2017), and by topology-based approaches (Tyukhova et al., 2015), while impacting the transverse dispersion (Cirpka et al., 2011, 2012). Such preferential pathways are known to contribute to the reaction patterns in reactive transport, as they vary the reactant concentration in space and time, for bimolecular reaction (Cirpka et al., 2012; Edery et al., 2010, 2016b), dissolution-precipitation reaction (Edery et al., 2011; Menke et al., 2018; Pereira Nunes et al., 2016; Yoon et al., 2019), and sorption (Raveh-Rubin et al., 2015). Their importance is also evident in vadose zones, where they affect contaminant distribution in soil (Ben--Noah et al., 2023; Hagedorn and Bundt, 2002), microbial communities in soil (Bundt et al., 2001; Kurz et al., 2022; Morales et al., 2010), lamella and mixing (Dentz et al., 2023) and even landslides (Hencher, 2010; Shao et al., 2015).

Preferential pathways may emerge even for the case of a uniform tracer front, which can then become funneled and split into distinct flowing branches (a schematic representation of the bifurcation is given in Fig. 1), a phenomenon known as channel branching (Fiori and Jankovic, 2012; Liao and Scheidegger, 1969; Moreno and Tsang, 1994; Torelli and Scheidegger, 1972). As a channel branches or as channels converge, in what is known as flow focusing (Ye et al., 2015), the tracer concentrations in each branch vary, leading to a non-uniform tracer flux that partially samples the conductivities in the domain. We refer to the location at which the preferential pathway channel splits into two as the bifurcation point, and the number of bifurcations over a domain cross-section as the bifurcation fraction. This bifurcation phenomenon was studied in similar fields, such as small-scale heat transfer bifurcation in porous media (Yang and Vafai, 2011a; 2011b), and bifurcations in braided rivers (Amooie et al., 2017; Bolla Pittaluga et al., 2003; Zolezzi et al., 2006). However, to date, no study has characterized the bifurcation of flow in porous media at the Darcy scale in the context of preferential pathways.

This work aims to describe these preferential pathway patterns and transport bifurcations on the Darcy scale. Here, we identify and characterize bifurcation points and under sampled regions (USR) using a particle tracking (PT) simulation that follows the local velocity. This local velocity is numerically calculated from a head difference applied on a conductivity field distributed lognormally in space, with a variance that marks a range from nearly homogeneous to highly heterogeneous distributions. We further show that the fraction of bifurcation out of the cross-section, decrease from inlet to outlet, reaching an asymptotic value that scales with the heterogeneity level, marked by the lognormal variance of the conductivity distribution. We identify a power-law correlation between the bifurcation and USR field fraction with the degree of variance of the lognormal conductivity distribution. Surprisingly, the same power-law captures the correlation between the heterogeneity and the transport tortuosity and characteristic fractal dimension. The same power-law correlation between the parameters and the variance is also apparent for a binary distribution of impermeable conductivities Moreover, as the degree of variance of the lognormal conductivity distribution is constant and the correlation length changes, the bifurcation fraction also changes with the correlation length, pointing to the complex role of correlation length.

## 2. Methods

### 2.1. Flow and transport modeling

We characterize the bifurcation of preferential pathways using a set of 2D numerical simulations, where a second-order stationary random domain of hydraulic conductivities, marked K from here on, is distributed according to a lognormal distribution with a mean of $\ln(K) \sim 0$ and an increasing heterogeneity level marked by a variance of $\sigma^2 = 1 - 7$, established by a sequential Gaussian simulator (GCOSIM3D) (Gómez-Hernández and Journel, 1993). This conductivity domain is composed of a mesh of $120 \times 300$ finite elements, referred to as conductivity bins (each of size $\Delta = 0.2$[cm], see schematic representation of a finite element bin in Fig. 1), forming a domain of $24 \times 60$ cm$^2$. Each domain is produced by a statistically homogeneous and isotropic Gaussian distribution in the ln(K), with a dimensionless

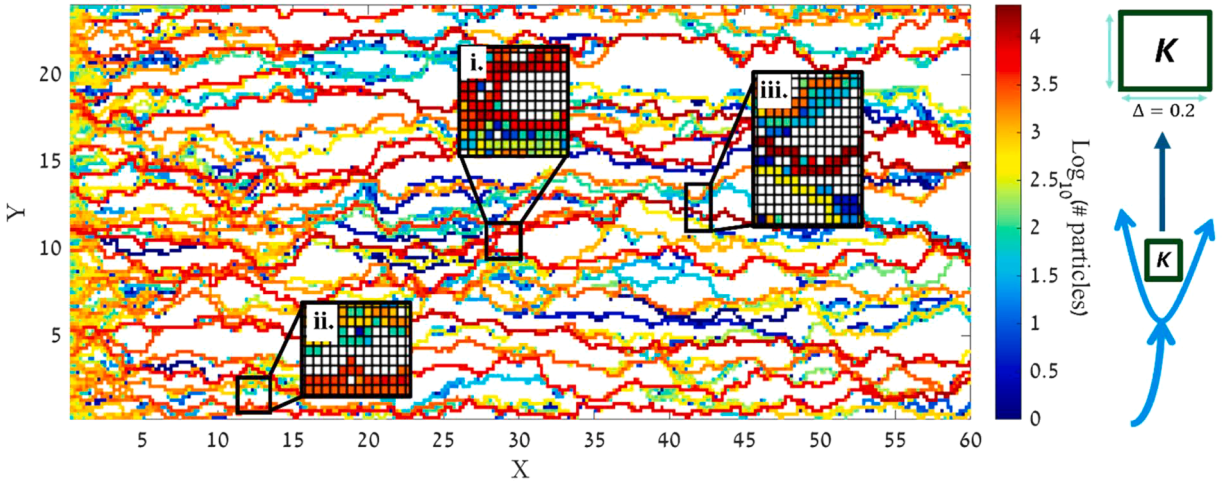


**Fig. 1.** Depiction of the number of particles visiting each bin throughout the simulation, on a logarithmic scale. White areas mark locations with no particle visitation; insets show examples of the following: i. Single bifurcation point where there are no particle visitations in the bifurcation point and downstream to it, while there are visits above and below the bifurcation point. ii. Bifurcation front, where multiple cells have no visitations. iii. Single stagnant point that is not defined as a bifurcation point. The right illustration depict the bifurcation around a conductivity bin, and the dimension of a finite element.

correlation length $l_c/L = 0.016$, where $L$ is the domain length along the main flow direction and $l_c$=1 [cm] is produced by an exponential covariance. This corresponds to a dimensionless value of $\Delta/l_c = 0.2$, which provides an accurate description of the small-scale fluctuations generated by the ln(K) domain and advective transport (Ababou et al., 1989; Riva et al., 2009) (see an example for the conductivity distribution in Fig. 2). To verify the effect of the correlation length, additional runs were performed over a larger mesh of 600 × 1500, taken from the center of domain the size of 1200 × 3000 to avoid boundary effects, with the same Δ and a range of correlation lengths ($l_c$=1–2.6 [cm]), providing a domain of 120 × 300 $cm^2$.

An ensemble of one hundred realizations are produced for each variance and correlation length, which was shown to be sufficient for statistical convergence of the first and second moments in a previous study (see Edery et al. (2014) for details). However, a new statistical convergence test was performed for this study, to quantity the number of realizations needed to reach the bifurcation fraction for the ensemble (see Fig. S1 in the supplementary information for details), following the convergence test done in Edery et al. (2021). Each realization had a deterministic pressure drop, which was translated to a total head drop ($H_{inlet\ -\ outlet}$ = 100[cm]), imposed from the inlet (left) to the outlet (right), and a finite element numerical model with a Galerkin weighting function that calculated the local head drop in 2D for each bin (Guadagnini and Neuman, 1999). The same simulation procedure in terms of correlation length, bin size, number of realizations, and variance range, is performed for $H_{inlet\ -\ outlet}$ = 10and1[cm], providing a range of Peclet number (*Pe)* values. Thus, the streamlines for each realization are retrieved, and from it, the local velocities are calculated using the local conductivity and porosity (θ=0.3). From the head difference and porosity, the Peclet number (*Pe)* can be defined as:

$$Pe = \frac{v_d\sqrt{K}}{\theta D_m} = \frac{v_d\sqrt{k\frac{\mu}{\rho g}}}{\theta D_m}, \quad (1)$$

where $v_d$ is the mean Darcy velocity calculated from the (arithmetic) average conductivity *K* and porosity θ, *k* the intrinsic permeability, μ and ρ the dynamic viscosity and density of water, respectively, g the gravity, and $D_m$ the diffusion of ions in water ($D_m = 10^{-5}\frac{cm^2}{sec}$) (Domenico and Schwartz, 1990). The ensuing value of *Pe* is indicative of an advection-dominated transport setup (see (Huysmans and Dassargues, 2005) for details). As the head drop ($H_{inlet\ -\ outlet}$) changes from 100 cm to 10 cm and then to 1 cm, the Darcy velocity ($v_d$) changes from 5.5 to 0.5 and then to 0.05 [cm/min], and the *Pe* from 597 to 59.7 and then to 5.97, respectively.

A PT simulation is employed to represent the transport of a tracer in the domain by tracking a pulse of particles ($np = 10^5$) per realization for each of the 100 realizations performed for each variance. These particles are distributed at the inlet according to the inlet conductivity distribution. At $t = 0$, the particle pulse starts to advance according to the local advection and diffusion term, following the Langevin equation:

$$\mathbf{d}_n = v[x_n(t)]\delta t + \mathbf{d}_{Dn}, \quad (2)$$

where $\mathbf{d}_n$ is the displacement, $x_n(t)$ is the known location of the n particle at time t, $v$ the fluid velocity at that location (v is the modulus of $|\mathbf{v}|$), $\delta t = \frac{\delta s}{v}$ the temporal displacement magnitude calculated from the fixed displacement size δs, and $\mathbf{d}_{Dn}$the diffusive displacement for particle n. The local fluid velocity field is obtained as $v = \mathbf{q}(\mathbf{x})/\theta$, where $\mathbf{q}(\mathbf{x})$ is the local Darcy flux:

$$\nabla\cdot\mathbf{q}(\mathbf{x}) = 0; \mathbf{q}(\mathbf{x}) = -K(\mathbf{x})\cdot\nabla h(\mathbf{x}) \quad (3)$$

The specific storage is neglected hereinafter in our steady state simulation for the flow, as there are no changes in the permeability field. The displacement size δs is selected to be an order of magnitude less than Δ to interpolate the velocity within each bin correctly. The PT simulation employed reflective boundary conditions, similar to a Dirichlet boundary condition, over the y-axis boundaries, and constant pressure boundary at the inlet and outlet, similar to the Neuman boundary condition, over the x-axis. To verify that the displacement size has no effect on the results obtained in this study, additional simulations for the same variances, yet with δs =Δ/100 proved to have no significant effect on the transport (Edery et al., 2014). The diffusive displacement, $\boldsymbol{d}_{Dn}$, is randomly generated for the x and y dimensions, whose entries are mutually independent and sampled from a Normal distribution between 0 and 1 ($\mathbf{N}[0, 1]$) multiplied by the square root of the diffusion coefficient and the temporal displacement magnitude, as illustrated in the following equation:

$$d_{Dn} = \mathbf{N}[0, 1]\sqrt{2D_m\delta t}. \quad (4)$$

The simulations were also run using $10^6$ particles and δs <Δ/10 with no significant numerical dispersion. The same GCOSIM3D model proved valuable in reproducing and analyzing field data (Eze et al., 2019; Obi

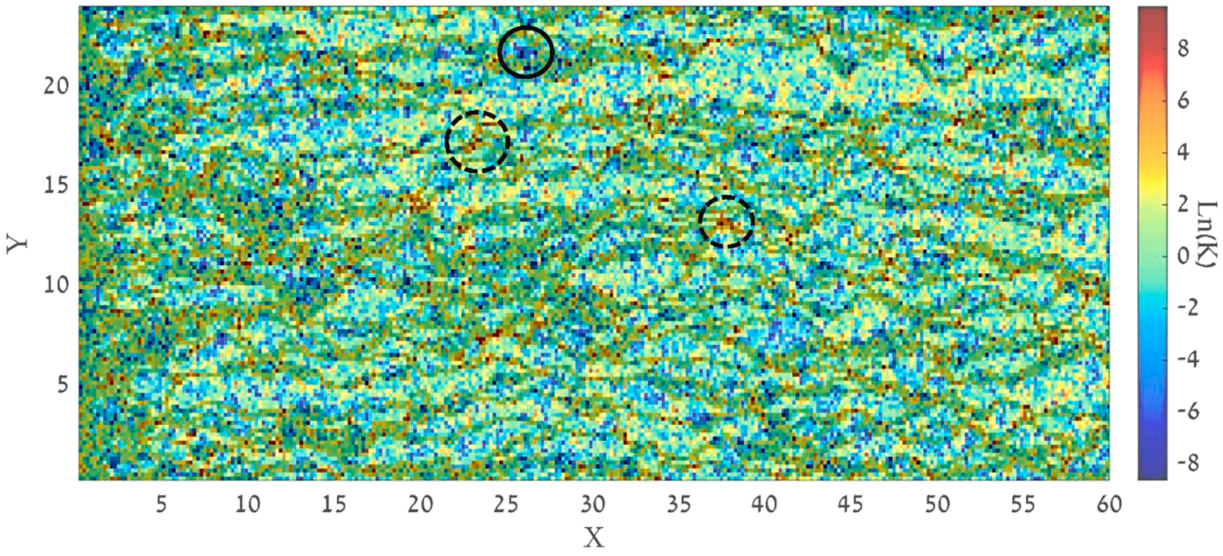


**Fig. 2.** Particle visitations number overlaid on the conductivity domain of a single realization with a variance of ln(K)= 5 and a color bar for ln(K). The darker hue describes the preferential pathways. The complete circle marks a bifurcation around a low conductivity area. The small, dashed circle marks a higher-than-average conductivity in which there is no transport. The bigger, dashed circle marks a higher-than-average conductivity that funnels the transport.

et al., 2020), uncertainty (Ciriello et al., 2013; Franssen et al., 2004; Riva et al., 2005), and upscaling (Li et al., 2011), while the PT method proved to be very robust and appropriate in this modeling configuration (Salamon et al., 2006; Salamon et al., 2006).

### 2.2. Defining the USR and bifurcations

While defining a bifurcation as the point where a channel splits into two is straightforward, searching for bifurcations within preferential pathways using specific criteria is more challenging. We, therefore, distinguish a set of points where the channel first splits while changing the flow direction tangentially. We define a bifurcation point as a cell with up-flow transport to it but no transport down-flow from it, although there is transport transversely to the down-flow direction (see example in Fig. 1i). For our PT simulation, the following condition can be used to identify a bifurcation:

$$C_{i,j} \le C_{th} \cup C_{\{(i-1,j),(i,j+1),(i,j-1)\}} > C_{th}, \tag{5}$$

where $C_{i,j}$ is the particle concentration at bin *i,j*, corresponding to the *x,y* dimensions, respectively, and $C_{th}$ the threshold concentration below which the bifurcation is established. In our simulations, $C_{th} = 0$, which is ~4 orders smaller than the mean particle value, $\widehat{C}$. The same $C_{th}$ determines the USR locations, as cells that are equal to or smaller than $C_{th}$; namely, $C_{i,j} \le C_{th}$. Other thresholds were employed ($C_{th}$= 1 and 10), providing similar results. This bifurcation definition can be adapted to a non-Lagrangian simulation using the same criteria, where $C_{th}$ is defined as $10^{-4}$ times the mean concentration of the tracer. In some cases, the bifurcation does not occur in a single cell, but rather in several vertically consecutive cells (i.e., in a bifurcation front), as shown in Fig. 1ii. Under this scenario, the definition in Eq. (3) is adjusted to be of the form:

$$C_{[(i,j),\ldots,(i,j+f)]} \le C_{th} \cup C_{\{([(i-1,j),\ldots,(i-1,j+f)]),(i,j+f+1),(i,j-1)\}} > C_{th}, \tag{6}$$

where *f* is the front length. This bifurcation front is typically ~1 % of all bifurcations and a maximum of 8 % of bifurcations per realization. This work does not consider bifurcation fronts because their occurrence is relatively negligible. In addition, as shown in Fig. 1iii., individual USR points are not defined in this work as bifurcation points, even though locally these points split the flow.

### 2.3. Defining the tortuosity and Hausdorff fractal dimension at the Darcy scale

In the Darcy scale model, the concept of advective tortuosity, as presented by Comolli et al. (2019), is the ratio between the displacement along the trajectory and the displacement along the flow direction ($\chi = \frac{\langle |\mathbf{q}(\mathbf{x})| \rangle}{\langle q_1(\mathbf{x}) \rangle}$). This property was found to increase monotonically with the heterogeneity of the medium. In this study, we calculate the tortuosity by measuring the trajectory length from inlet to outlet for each simulated particle ($T_n$) and dividing it by the domain length ($T_n/L$). By doing so for all the particles, we obtain the mean tortuosity for each realization:

$$f_{Tort} = \left( \sum_{i=1}^{\mathrm{np}} T_i \Big/ L \right) \Big/ \mathrm{np}. \tag{7}$$

The tortuosity within the pore scale is often related to permeability using a fractal dimension (Xia et al., 2018; Yu and Cheng, 2002; Yu and Liu, 2004), which bears a resemblance to our analysis, as the averaging of the tortuous preferential pathways provides the weighting of the conductivities by the amount of particles sampling each conductivity, that differs from the arithmetic average conductivity, as presented in ( Edery et al. (2014). As such, as the particles trajectories sample the domain in an incomplete, tortuous way, the trajectories self-similarity, we calculate the Hausdorff fractal dimension (Hfd) at the Darcy scale using the box-counting method, as suggested in (Falconer, 1988; Moisy, 2008). To calculate the Hfd using the box-counting method, images like the one in Fig. 1 are translated to a binary image, followed by marking as 1 each bin where at least one particle visited throughout the simulation, and as 0 otherwise. This binary image is divided into b boxes of equal size *s*. Next, the sum of boxes with at least one 1 ($N(b)$) is extracted for each box size.

$$Hfd\ (r) = \frac{\left(Ln(\left[\sum_{i=1}^{b(s=2)} N(b) > 0, \ldots, \sum_{i=1}^{b(s=120)} N(b) > 0\right)\right.}{Ln([b(s=1), \ldots, b(s=120)]}. \tag{8}$$

By repeating the process for all possible box sizes, a grid of evenly distributed boxes is generated, the slope of which relates the logarithm to the sum of 1 s divided by the logarithm of the total boxes is the Hfd. Similar computational methods were developed by Costa et al. (2012), Moisy (2008). This calculation is done for all the ensembles per variance, resulting in a mean Hfd for each variance.

## 3. Results

In the following, we identify and characterize the bifurcation, from inlet to outlet, for domains with varying heterogeneity levels (Section 3.1). We show how heterogeneity affects the topology of preferential pathways and demonstrate that the correlations between the bifurcation to the heterogeneity can be captured by a power-law. A power law with similar exponent can capture the correlations of the USR, tortuosity, and fractal dimension of the preferential pathways with the heterogeneity of the domain (Section 3.2). Moreover, the same power law captures the correlations between a distribution of close to impermeable conductivities randomly distributed within a permeable, uniform conductivity domain, and the stated parameters (Section 3.3). We then extend our analysis to variations in the correlation length, $l_c$ (Section 3.4).

### 3.1. Analyzing bifurcation distribution for various heterogeneity and Pe

While we established the definition of bifurcations for this study, the mechanism originating from the flow and tracer transport through the conductivity domain, that leads to these bifurcations, is not clearly characterized. In the simplified case where there is a non-conductive impermeable region within a conductive area, it is evident that a bifurcation bypassing the impermeable region will occur, making it a local event. However, bifurcations mainly occur upstream around locations with low conductivity, in a way that maximizes the path of least resistance globally. Evidence for this kind of bifurcation around a low conductive area can be found in Levy and Berkowitz (2003). They showed that while the tracer branches around low hydraulic conductivity zones, some of it does enter these zones, as it serves the overall minimization of flow through the global solution of transport, as shown in Zehe et al. (2021). This branching of transport is presented in Fig. 3; the temporal and spatial evolution of the pulse tracer exhibits similar behavior to that in our simulations, as shown by Berkowitz (2021). The preferential pathways are marked by a substantial spatial change in the tracer concentration from inlet to outlet, at all scales. Yet, relating the preferential pathway structure to the “resistance mechanism”, which is calculated from the Darcy scale, has not yet been achieved.

These preferential pathway funnel towards higher conductivities while bifurcating around low conductivities (Fig. 2), forming a path of least resistance. As such, the ratio between the conductivities at the bifurcation point and at the downstream point where there are no particle visitations should be consistently higher than one. Yet a substantial portion of the histogram of these bifurcation ratios is smaller than one (Fig. 4), pointing to a global, not local, minimization of energy for the transport. Nonetheless, the histogram ratio is, on average, smaller than one and it scales with the conductivity variance of the domain (Fig. 5a), calculated for all the ensemble realizations. Moreover, the Peclet number, which relates diffusion to velocity (Eq. (1)), has only a limited influence on the bifurcation ratio, when the conductivity upstream from

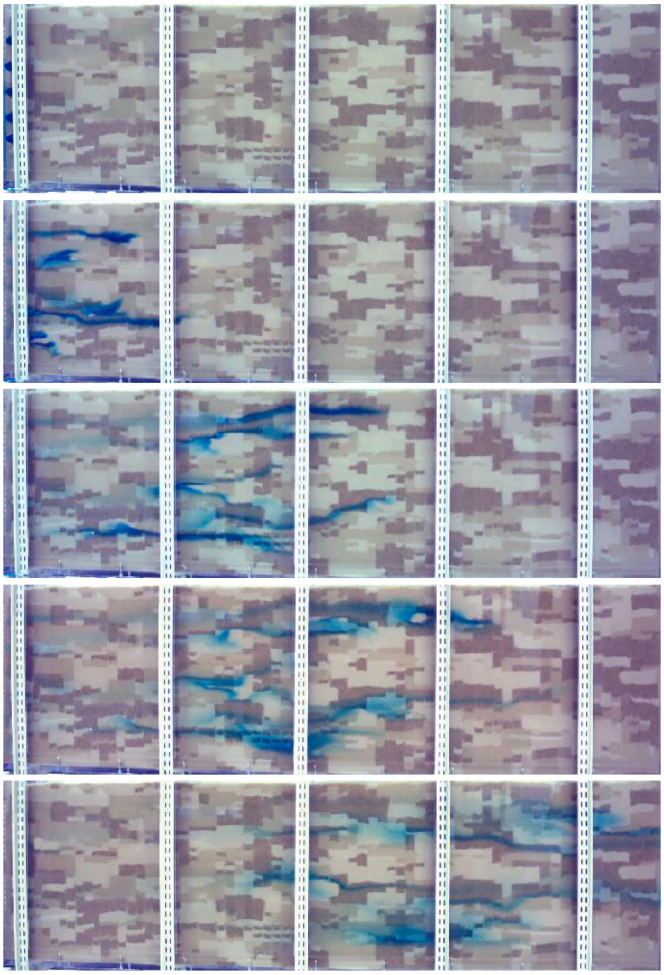

**Fig. 3.** Images of the randomly heterogeneous medium used in (Levy and Berkowitz, 2003) with five dye tracer point injections being transported, under constant flow from left to right, as seen through the front wall. The brown, light-brown and white depict high, medium, and low conductivity sands distributed in an exponentially correlated structure, in a flow cell of 213 × 65 × 10 cm. modified from ( Levy and Berkowitz, 2003; © with permission from Elsevier 2003.

the bifurcation (dashed, blue line) is compared with the conductivity downstream from the bifurcation (solid, black line), as well as in relation to the domain conductivity distribution (red circles), as can be seen in Fig. 4. Nonetheless, we anticipate that in an extremely diffusion-dominated system, preferential pathways and, therefore, bifurcations, will become less dominant, eventually disappearing altogether with an increased component of diffusion.

Fig. 1 further shows that there are more bifurcations in the upstream locations than in downstream ones, due to the continuous funneling of separate preferential pathway channels, making them more distinct downstream. This issue is also addressed in Zehe et al. (2021), which shows that the entropy declines towards an asymptote due to the additional funneling of preferential pathways, a process exacerbated as the heterogeneity of the conductivity distribution, marked by the distribution variance, increases. This downstream reduction in the mean bifurcation is apparent in the bifurcation fraction over the y-axis, averaged over the ensemble, with an initial increase in the number of bifurcations, followed by a decrease towards an asymptote for all variances (Fig. 5b). It seems that the maximum bifurcation fraction is 0.035 for all variances. Yet, the asymptotic value becomes smaller as the variance increases, indicating that the number of distinct preferential pathways decreases with the increase in variance, through this funneling mechanism (Fig. 5b. inset).

### 3.2. Scaling of bifurcations, USR, tortuosity, and the Hausdorff dimension with heterogeneity

As seen in Fig. 5b., the bifurcation fraction asymptotic value decreases with the increase in variance, in a declining form. To quantify this decline, we plot the bifurcation fraction asymptotic value ($f_{Bif}$) against the variance ($\sigma^2$) divided by the square of correlation length ($l_c^2$) for dimensionality purposes, and see that a power law captures this declining rate:

$$f_{Bif} = 0.027 \cdot \left(\sigma^2 / l_c\right)^{-0.25} - 0.0057, \tag{9}$$

see Fig. 6a. for details. This correlation of the bifurcations to an asymptotic value occurs within ten realizations and does not vary much thereafter, as can be seen in Supplementary Fig. S1. Moreover, the variance between different realizations forming the ensemble of the bifurcation fraction, decreases with the increase in the variance of the conductivity lognormal distribution. This reduction in variance follows the streamline analysis in Supplementary Fig. S2, which shows how the number of preferential pathways and streamlines decreases with the lognormal conductivity variance.

According to the definition of bifurcation, each bifurcation leads to the formation of a USR where there is either no particle visitation or an extremely low tracer concentration, as can be seen in Figs. 1 and 3, respectively (Berkowitz, 2021; Levy and Berkowitz (2003). This suggests that there should be a relation between the USR fraction in the domain and the lognormal conductivity variance. Indeed, the USR fraction increases with the lognormal conductivity variance, mirroring the bifurcation fraction trend (Fig. 6a). This increase in USR fraction ($f_{USR}$) can be captured with the same power as that of the bifurcation fraction pattern, namely:

$$f_{USR} = -0.564 \cdot \left(\sigma^2 / l_c\right)^{-0.25} + 1, \tag{10}$$

where the asymptotic value 1 is for an infinite heterogeneity variance that forms a single channel from inlet to outlet with no bifurcation and maximum USR. This analysis points to a relation between the bifurcation and the formation of USR or areas where transport is diffusion-dominated; this relation scales with the variance of the domain. The existence of a USR fraction in a Darcy scale simulation that scales with the variance points to the preferential pathways being tortuous on the Darcy scale and being the outcome of the USR and bifurcation.

Using the calculated tortuosity presented in Section 2.3, we find the same power law correlation between the tortuosity and variance:

$$f_{Tort} = 0.014 \cdot \left(\sigma^2 / l_c\right)^{d-0.25} + 1, \tag{11}$$

where 1 is the tortuosity for a completely uniform domain ($\sigma^2 = 0$), and $d = 2$ is the dimension of the domain (Fig. 6b). The concept of streamline tortuosity ($\chi$) was presented in Comolli and Dentz (2017) and Comolli et al. (2019), and we obtain values similar to those in their simulations (blue axes in Fig. 6b). Yet, our direct measurement of the tortuosity is weighted by the number of particles occupying each trajectory, which scales the tortuosity value by the flux of each trajectory.

The relation between tortuosity and heterogeneity variance suggests that the preferential pathways can be described by the same power law. Studies often use a fractal dimension to connect tortuosity to permeability (Xia et al., 2018; Yu and Cheng, 2002; Yu and Liu, 2004), which bears a resemblance to our analysis, as the fractal dimension describing the bifurcating tortuous preferential pathways in the domain is the outcome of the conductivities weighted by the particle visitation that differs from the arithmetic average conductivity, as presented in Edery et al., (2014). As such, we calculate the Hfd, following the boxcount method presented in Section 2.3, and show that there is a relation

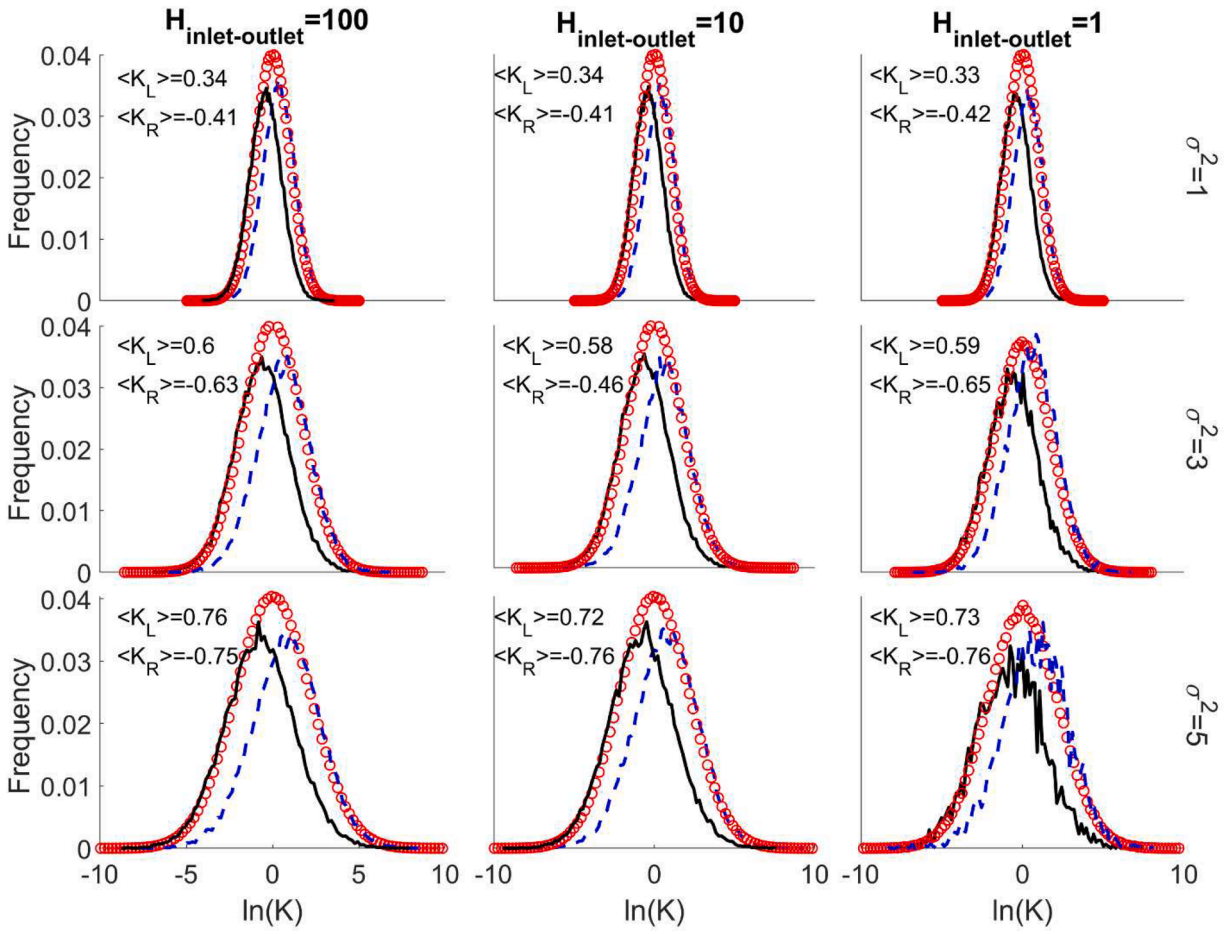


**Fig. 4.** Frequency of the lognormal conductivity for an ensemble of domains (red circles), the conductivity upstream to the bifurcation (dashed, blue line), and the conductivity downstream from the bifurcation (solid, black line); boxes present the average values. Results correspond to $\Delta h = 100, 10, 1$(left, middle and right columns, respectively), and to $\sigma_0^2 = 1, 3, 5$ (upper, middle, and bottom rows, respectively, with the same x-axis per figure column).

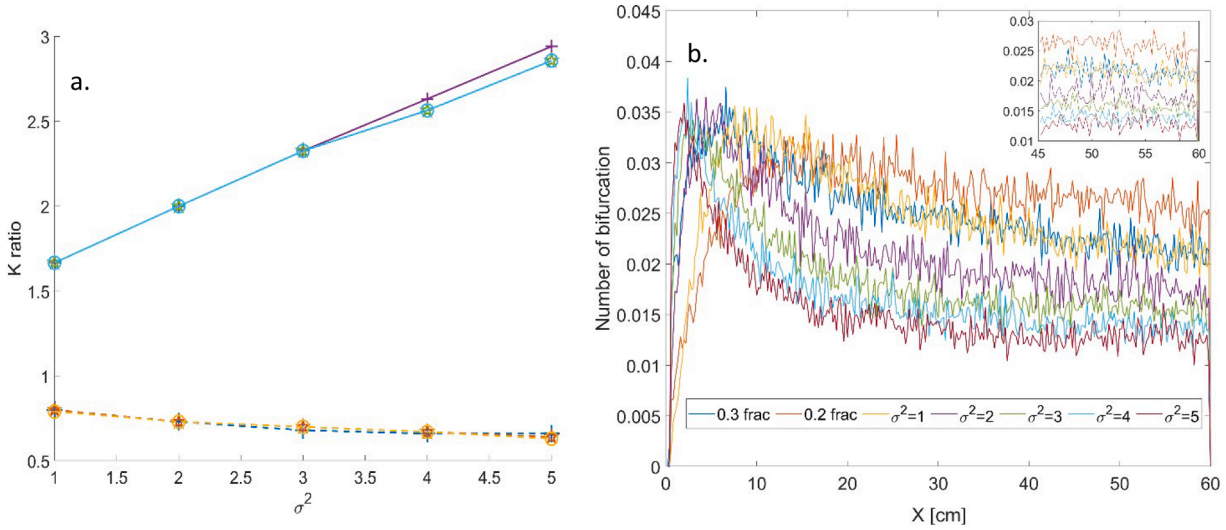


**Fig. 5.** a. Mean conductivity ratio marks the average ratio between the conductivity of the bin upstream from the bifurcation point and the conductivity at the bifurcation point (solid line), and the conductivity of the bin downstream from the bifurcation point and the conductivity at the bifurcation point (dashed line). This analysis is performed for head values of 1, 10 and 100 (plus, pentagram and circle signs, respectively), as a function of the heterogeneity ($\sigma^2$). While there is a distinct difference between the conductivity ratio before and after the bifurcation for both the value and the trend, the head difference has little effect on them, pointing to the robustness of the bifurcation characteristics. b. Bifurcation fraction marks the ratio of bifurcation points along the y-axis divided by the total number of cells along the y-axis, averaged over the ensemble realizations, versus the x-axis. Each color represents a different heterogeneity level captured by the variance, yet all reach an asymptotic value, shown in the inset.

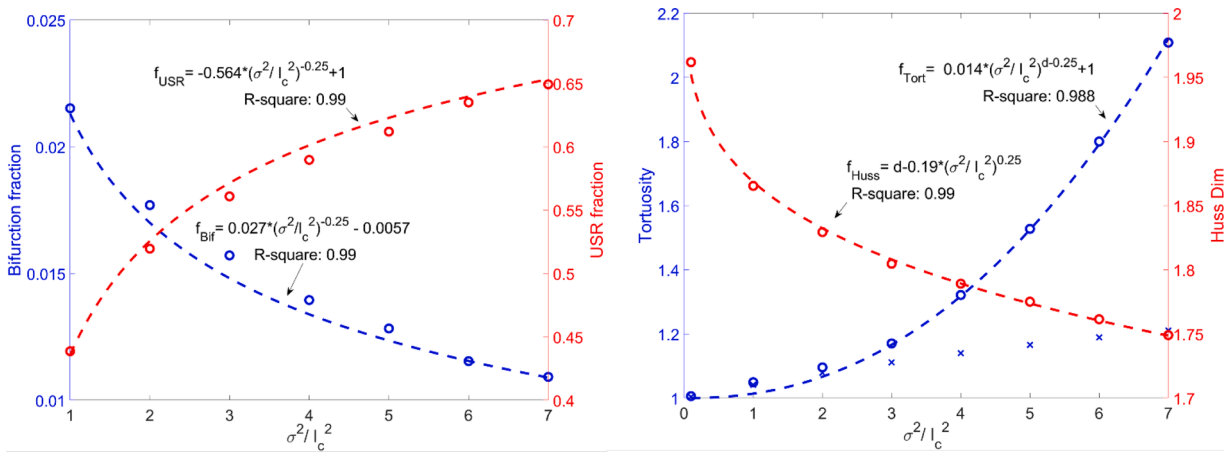


**Fig. 6.** a. Mean bifurcation fraction, taken from the asymptotic value in Fig. 5b., as conductivity variance increases (blue circles) and a power-law fit (dashed, blue line). Mean USR fraction (red circles) as the conductivity variance increases, with its power-law fit (dashed, red line). b. Mean tortuosity value, calculated from the particle trajectory, as the conductivity variance increases (blue circles), and its power-law fit, where the dimension is marked by $d = 2$ (dashed, blue line), while the streamline tortuosity suggested by Comolli and Dentz (2017) and Comolli et al. (2019) are marked by blue axes. The mean Hausdorff fractal dimension as the conductivity variances increases (red circles), and its power-law fit (dashed, red line).

between the Hfd and the variance, following the same power law correlation:

$$f_{Huss} = d - 0.14 \cdot \left(\sigma^2 / l_c\right)^{0.25}, \tag{12}$$

where $d = 2$ is the dimension of the domain, which is also the fractal dimension for a completely uniform domain (Fig. 6b). The variance for the bifurcation fraction, USR fraction, tortuosity and Hfd is very narrow and converges very quickly with each added iteration of the simulation ensemble (Supplementary Fig. S2).

### 3.3. Scaling of bifurcations, USR, tortuosity and Hausdorff dimension with binary conductivity distribution

We repeated the same analysis for a domain with a single bulk conductivity, while distributing various volume fractions of conductivity bins that are 6 orders of magnitude lower than the domain bulk conductivity, which effectively makes them impermeable; these regions will be referred hereafter as impermeable bins. The impermeable bins are uniformly distributed, forming a fraction 0.05 to 0.2 from the total domain, thus providing a binary distribution of conductivities. The nature of the impermeable fraction does not allow flow through a fraction of the domain, leading to a linear increase in the USR fraction. Yet the same power-law correlation for the bifurcation fraction, tortuosity and Hausdorff dimension with the impermeable fraction still emerges, as can be seen in Fig. 7. Due to the nature of this binary system—namely, that the ratio of impermeable areas increases while there is but a single permeable value that is uncorrelated—the ratio of bifurcations increases as a power-law to an asymptote. From that asymptote, an increase in the impermeable fraction leads to a critical obstacle layout that does not allow percolation (Stauffer and Aharony, 2018). While the power law parameters which correlate the bifurcation fraction, tortuosity and Hausdorff dimension with the impermeable fraction differ from the lognormal variance in Section 3.2, the power law relation retain the same exponent.

### 3.4. Scaling of bifurcation, USR, tortuosity and the Hausdorff dimension with correlation length

We performed a similar analysis for various increases in the correlation length ($l_c$), for a mean conductivity of $\sigma^2 = 5$. Increasing the correlation length led to larger inclusions of low and high conductivity areas (Edery, 2021), which caused a marked decrease in the bifurcation fraction (Figs. 8 and 9a) and a respective increase in void formation (Fig. 9a). Yet this increase in the inclusions with the correlation length does not scale as in the variance change case, which is to be expected

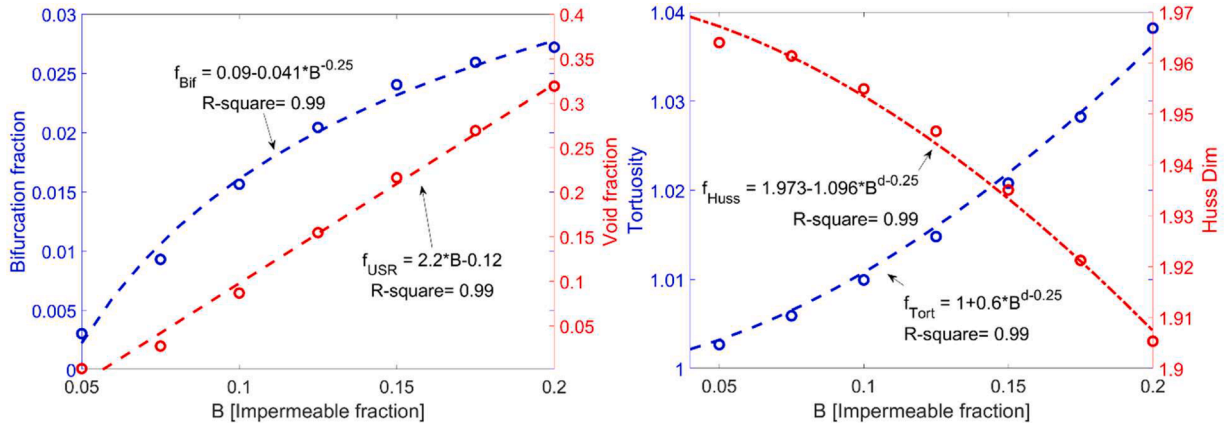


**Fig. 7.** a. The mean bifurcation (blue) and USR (red) fraction values (circles), taken from the asymptotic value, as the impermeable area increases and their respective power-law fit (dashed lines). b. Mean tortuosity value (blue) and Hausdorff fractal dimension (red), calculated from particle trajectories, as the impermeable area increases, and their respective power-law fit (dashed lines).

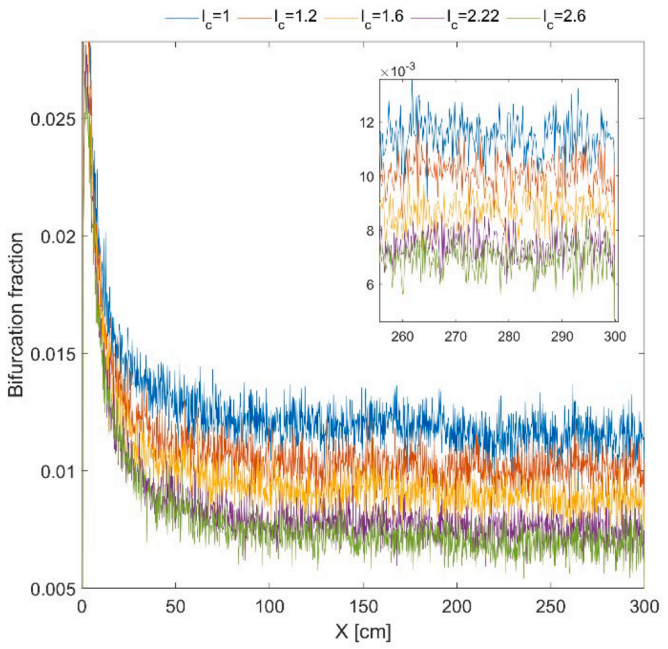


**Fig. 8.** Bifurcation fraction along the *y*-axis, for each bin of the *x*-axis. Each color represents a different correlation length value, leading to a decreasing asymptotic value with the increase in correlation length as shown in the inset.

since the overall heterogeneity, marked by the variance, is not changed. While we do apply a trend line that follows a power law (equations in Fig. 9a), the exponents are different. However, the same trend of a decreasing bifurcation and an increasing USR still holds. Moreover, the same trend of increase in tortuosity and decrease in the fractal dimension is also observed when the length is increased (Fig. 9b. and equation within).

## 4. Summary and conclusions

In this study, we define and analyze the role of transport bifurcation and show that while transport and bifurcation locations occur at higher-than-average conductivities and bypass low conductivities, bifurcations also occur around high conductive areas, following the path of least resistance for the total transport and not the local scale. While the splitting of a channel is implicitly known to be partially responsible for non-Fickian transport, the bifurcation has yet to be related to the heterogeneity, to the best of our knowledge. The main findings are:

- The bifurcation correlates with the heterogeneity variance following a power law, and lead to USR formation, areas where there are no particle visitations in the domain that can be fitted with similar power law. Both the bifurcations and USR formations can be addressed similarly in concentration-based simulations by establishing a cut-off to the local concentration that corresponds to the particle concentration.
- The direct tortuosity measurement, weighted by the particle concentration, is captured by the same power law found for the bifurcation and USR fraction, yet it differs from the advection tortuosity scaling suggested in Comolli et al. (2019) in the context of streamline tortuosity.
- The Hfd fractal dimension analysis for the preferential pathways, which captures the tortuosity, bifurcation and USR, correlates with the variance with similar power law fit. Therefore, the bifurcation fraction, USR fraction, tortuosity and fractal dimension independently correlate with the variance as a power law with similar exponent.
- A similar analysis performed for the binary case, with an impermeable fraction, offered the same power law correlation with the impermeable fraction, and similar exponent for all but the USR fraction, pointing to the robustness of this correlation.
- Analyzing the correlation length proved that the same trends of Hfd, tortuosity, bifurcation and USR hold for the correlation length increase, yet not with the same power law exponent for all the suggested parameters. We believe that as the correlation length parameter differs from the heterogeneity, marked by the variance, so should the dependency of the exponent.

### 4.1. Discussion

The value of the exponent for the power law that defines this correlation between heterogeneity variance and the presented parameters is the only value that fits all of the relations between the variance and the bifurcation, USR fraction, tortuosity and Hfd, leaving but one fitting parameter. Yet the fact that there is an exponent common to all preferential pathway characteristics indicates that the optimization of transport in a conductive domain leads to a geometrical pattern of preferential pathways that is manifested by these parameters. We

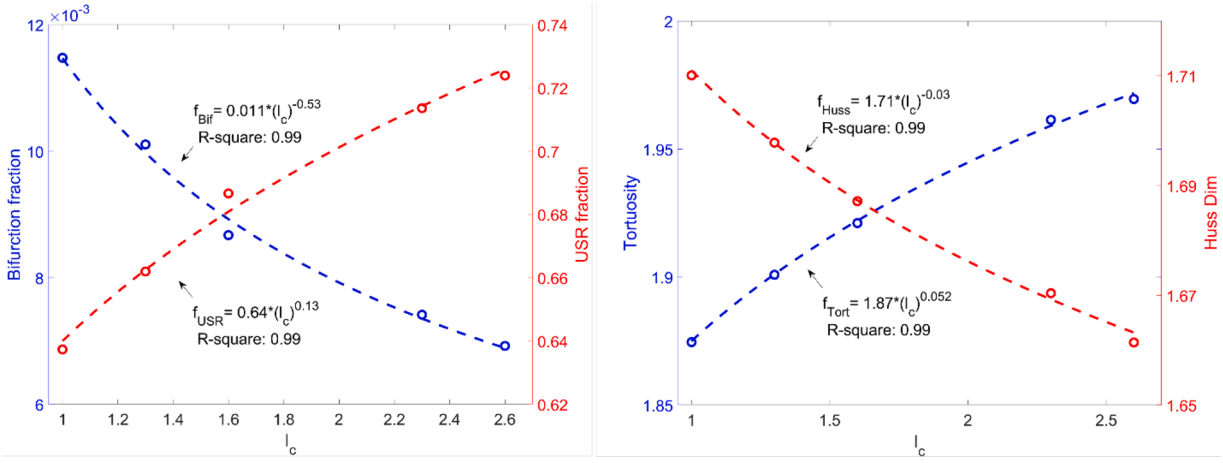


**Fig. 9.** a. Mean bifurcation fraction, taken from the asymptotic value taken from the larger fields (600 × 1500), for a conductivity variance of 5, and a correlation length $l_c$=1–2.6 (blue circles), with a power-law fit (blue dashed line). Mean USR fraction (red circles) as correlation length increases, with its power-law fit (red dashed line). b. Mean tortuosity value, calculated from particle trajectory, as correlation length increases (blue circles), and its power-law fit (blue dashed line). Mean Hausdorff fractal dimension as conductivity variances increases (red circles), and its power-law fit (red dashed line).

further speculate that increasing the dimension to a 3D model will provide similar results that follow a power-law correlation, yet not with the same exponent. Our speculation is based on the similarity between the preferential pathway behavior to Percolation theory, as pointed out by Hunt and Sahimi (2017), and by experimental indications on the increased dominance of preferential pathways (Bianchi et al., 2011). As the bond percolation on a square lattice decreases from 0.5 in 2D to 0.248 in 3D (as proven by Kesten (1982)), or from a site percolation of 0.59 in 2D to 0.311 in 3D, we will expect that the governing exponent will change in our preferential pathway analysis, but not the overall characteristics. While this change is dependent on the lattice used, it is persistent in nature, as indicated by our analysis for larger domains. Our simulations do not deal with percolation, as there is no real limitation for the transport as in a percolation system, but rather a range of resistance to the flow, established by the range of hydraulic conductivities. Therefore, we expect the bifurcation fraction magnitude to remain similar to the USR fraction versus x-axis, yet with a higher scale for the reduced value of bifurcations, and increase the USR versus heterogeneity, since the optimization for the path of least resistance has an additional dimension to percolate through as we move from a 2D to a 3D system.

While the tortuosity, USR and bifurcations are apparent in experimental setups (Bianchi et al., 2011; Levy and Berkowitz, 2003), the preferential pathway pattern is not characterized experimentally in the literature since it is challenging to quantify a tracer pulse trajectory in a Darcy scale experimental setup. Nonetheless, the correlation found here may have implications for many disciplines of porous media research, from contaminant transport (Edery, 2021; Edery et al., 2016a, 2014; Hagedorn and Bundt, 2002; Zehe et al., 2021), where the contamination location follows the preferential pathway, to reactive transport, where the reaction is set by the reactant concentration that follows the preferential pathways (Edery et al., 2011, 2015, 2021; Edery et al., 2016b; Raveh-Rubin et al., 2015). Moreover, there are indications that bacteria in soils not only rely on these preferential pathways (Bundt et al., 2001) but actually form them (Morales et al., 2010).

## Data and software availability

This work does not include any experimental data. The codes and analysis are included in a dedicated repository (*Edery*, 2023).

## Author agreement statement

We the undersigned declare that this manuscript is original, has not been published before and is not currently being considered for publication elsewhere.

We confirm that the manuscript has been read and approved by all named authors and that there are no other persons who satisfied the criteria for authorship but are not listed. We further confirm that the order of authors listed in the manuscript has been approved by all of us.

We understand that the Corresponding Author is the sole contact for the Editorial process. He/she is responsible for communicating with the other authors about progress, submissions of revisions and final approval of proofs

## CRediT authorship contribution statement

**Avioz Dagan:** Writing – original draft, Software, Methodology, Investigation, Formal analysis, Data curation. **Yaniv Edery:** Writing – review & editing, Writing – original draft, Supervision, Software, Resources, Project administration, Investigation, Funding acquisition, Conceptualization.

## Declaration of competing interest

The authors declare the following financial interests/personal relationships which may be considered as potential competing interests:

Yaniv Edery reports financial support was provided by Israel Science Foundation.

## Data availability

No data was used for the research described in the article.

## Acknowledgments

Y.E. and A.D. thank the support of ISF-NSFC (Grant No. 3333/19).

## Supplementary materials

Supplementary material associated with this article can be found, in the online version, at doi:10.1016/j.advwatres.2024.104622.

## References

Ababou, R., McLaughlin, D., Gelhar, L.W., Tompson, A.F.B., 1989. Numerical simulation of three-dimensional saturated flow in randomly heterogeneous porous media. Transp. Porous Media 4 (6), 549–565. https://doi.org/10.1007/bf00223627.
Amooie, M.A., Soltanian, M.R., Moortgat, J., 2017. Hydrothermodynamic mixing of fluids across phases in porous media. Geophys. Res. Lett. 44 (8), 3624–3634. https://doi.org/10.1002/2016GL072491.
Bear, J., 2013. Dynamics of Fluids in Porous Media. Courier Corporation.
Ben-Noah, I., Hidalgo, J.J., Jimenez-Martinez, J., Dentz, M., 2023. Solute trapping and the mechanisms of Non-Fickian transport in partially saturated porous media. Water Resour. Res. 59 (2), e2022WR033613.
Berkowitz, B., 2021. HESS opinions: chemical transport modeling in subsurface hydrological systems–Space, time, and the holy grail of "upscaling". Hydrol. Earth Syst. Sci. Discuss. 1–31.
Berkowitz, B., Scher, H., 1997. Anomalous transport in random fracture networks. Phys. Rev. Lett. 79 (20), 4038.
Bianchi, M., Zheng, C., Wilson, C., Tick, G.R., Liu, G., Gorelick, S.M., 2011. Spatial connectivity in a highly heterogeneous aquifer: from cores to preferential flow paths. Water Resour. Res. 47 (5).
Bijeljic, B., Raeini, A., Mostaghimi, P., Blunt, M.J., 2013. Predictions of non-Fickian solute transport in different classes of porous media using direct simulation on pore-scale images. Phys. Rev. E 87 (1), 013011.
Bolla Pittaluga, M., Repetto, R., Tubino, M., 2003. Channel bifurcation in braided rivers: equilibrium configurations and stability. Water Resour. Res. 39 (3).
Bundt, M., Widmer, F., Pesaro, M., Zeyer, J., Blaser, P., 2001. Preferential flow paths: biological 'hot spots' in soils. Soil Biol. Biochem. 33 (6), 729–738.
Ciriello, V., Di Federico, V., Riva, M., Cadini, F., De Sanctis, J., Zio, E., Guadagnini, A., 2013. Polynomial chaos expansion for global sensitivity analysis applied to a model of radionuclide migration in a randomly heterogeneous aquifer. Stoch. Environ. Res. Risk Assess. 27 (4), 945–954.
Cirpka, O.A., Kitanidis, P.K., 2000. Characterization of mixing and dilution in heterogeneous aquifers by means of local temporal moments. Water Resour. Res. 36 (5), 1221–1236.
Cirpka, O.A., de Barros, F.P., Chiogna, G., Rolle, M., Nowak, W., 2011. Stochastic flux-related analysis of transverse mixing in two-dimensional heterogeneous porous media. Water Resour. Res. 47 (6).
Cirpka, O.A., Rolle, M., Chiogna, G., De Barros, F.P., Nowak, W., 2012. Stochastic evaluation of mixing-controlled steady-state plume lengths in two-dimensional heterogeneous domains. J. Contam. Hydrol. 138, 22–39.
Comolli, A., Dentz, M., 2017. Anomalous dispersion in correlated porous media: a coupled continuous time random walk approach. Eur. Phys. J. B 90 (9), 166.
Comolli, A., Hakoun, V., Dentz, M., 2019. Mechanisms, upscaling, and prediction of anomalous dispersion in heterogeneous porous media. Water Resour. Res. 55 (10), 8197–8222.
Costa, A.F., Humpire-Mamani, G., Traina, A.J.M., 2012. An efficient algorithm for fractal analysis of textures. In: Proceedings of the Paper Presented at 25th SIBGRAPI Conference on Graphics, Patterns and Images. IEEE.
Cushman, J.H., Ginn, T., 1993. Nonlocal dispersion in media with continuously evolving scales of heterogeneity. Transp. Porous Media 13 (1), 123–138.
Dentz, M., Hidalgo, J.I., Lester, D., 2023. Mixing in porous media: concepts and approaches across scales. Transp. Porous Media 146 (1), 5–53.
Domenico, P., Schwartz, F., 1990. Physical and Chemical Hydrogeology, Edited. John Wiley and Sons, New York.
Dullien, F.A., 2012. Porous Media: Fluid Transport and Pore Structure. Academic press.
Edery, Y., 2021. The effect of varying correlation lengths on anomalous transport. Transp. Porous Media 137 (2), 345–364.
Edery, Y. (2023), Bifurcation data, https://zenodo.org/badge/630338056.svg.
Edery, Y., Scher, H., Berkowitz, B., 2010. Particle tracking model of bimolecular reactive transport in porous media. Water Resour. Res. 46 (7).
Edery, Y., Scher, H., Berkowitz, B., 2011. Dissolution and precipitation dynamics during dedolomitization. Water Resour. Res. 47 (8).

Edery, Y., Geiger, S., Berkowitz, B., 2016a. Structural controls on anomalous transport in fractured porous rock. Water Resour. Res. 52 (7), 5634–5643.
Edery, Y., Weitz, D., Berg, S., 2018. Surfactant variations in porous media localize capillary instabilities during Haines jumps. Phys. Rev. Lett. 120 (2), 028005.
Edery, Y., Guadagnini, A., Scher, H., Berkowitz, B., 2014. Origins of anomalous transport in heterogeneous media: structural and dynamic controls. Water Resour. Res. 50 (2), 1490–1505.
Edery, Y., Dror, I., Scher, H., Berkowitz, B., 2015. Anomalous reactive transport in porous media: experiments and modeling. Phys. Rev. E 91 (5), 052130.
Edery, Y., Stolar, M., Porta, G., Guadagnini, A., 2021. Feedback mechanisms between precipitation and dissolution reactions across randomly heterogeneous conductivity fields. Hydrol. Earth Syst. Sci. Discuss. 1–14.
Edery, Y., Porta, G.M., Guadagnini, A., Scher, H., Berkowitz, B., 2016b. Characterization of bimolecular reactive transport in heterogeneous porous media. Transp. Porous Media 115 (2), 291–310.
Eze, P.N., Madani, N., Adoko, A.C., 2019. Multivariate mapping of heavy metals spatial contamination in a Cu–Ni exploration field (Botswana) using turning bands co-simulation algorithm. Nat. Resour. Res. 28 (1), 109–124.
Falconer, K.J., 1988. The Hausdorff dimension of self-affine fractals. In: Proceedings of the Paper Presented at Mathematical Proceedings of the Cambridge Philosophical Society. Cambridge University Press.
Fasano, A., Talamucci, F., 2000. A comprehensive mathematical model for a multispecies flow through ground coffee. SIAM J. Math. Anal. 31 (2), 251–273.
Fiori, A., Jankovic, I., 2012. On preferential flow, channeling and connectivity in heterogeneous porous formations. Math. Geosci. 44 (2), 133–145.
Franssen, H.H., Stauffer, F., Kinzelbach, W., 2004. Influence of uncertainty of mean transmissivity, transmissivity variogram and boundary conditions on estimation of well capture zones. GeoENV IV—Geostatistics For Environmental Applications, Edited. Springer, pp. 223–234.
Gómez-Hernández, J.J., Journel, A.G., 1993. Joint sequential simulation of multigaussian fields. Geostatistics Troia'92, Edited. Springer, pp. 85–94.
Guadagnini, A., Neuman, S.P., 1999. Nonlocal and localized analyses of conditional mean steady state flow in bounded, randomly nonuniform domains: 1. Theory and computational approach. Water Resour. Res. 35 (10), 2999–3018. https://doi.org/10.1029/1999wr900160.
Hagedorn, F., Bundt, M., 2002. The age of preferential flow paths. Geoderma 108 (1–2), 119–132.
Haggerty, R., McKenna, S.A., Meigs, L.C., 2000. On the late-time behavior of tracer test breakthrough curves. Water Resour. Res. 36 (12), 3467–3479.
Haggerty, R., Fleming, S.W., Meigs, L.C., McKenna, S.A., 2001. Tracer tests in a fractured dolomite: 2. Analysis of mass transfer in single-well injection-withdrawal tests. Water Resour. Res. 37 (5), 1129–1142.
Hakoun, V., Comolli, A., Dentz, M., 2019. Upscaling and prediction of Lagrangian velocity dynamics in heterogeneous porous media. Water Resour. Res. 55 (5), 3976–3996.
Hencher, S., 2010. Preferential flow paths through soil and rock and their association with landslides. Hydrol. Process 24 (12), 1610–1630.
Hunt, A.G., Sahimi, M., 2017. Flow, transport, and reaction in porous media: percolation scaling, critical-path analysis, and effective medium approximation. Rev. Geophys. 55 (4), 993–1078.
Huysmans, M., Dassargues, A., 2005. Review of the use of Péclet numbers to determine the relative importance of advection and diffusion in low permeability environments. Hydrogeol. J. 13 (5), 895–904.
Kang, P.K., Dentz, M., Le Borgne, T., Juanes, R., 2011. Spatial Markov model of anomalous transport through random lattice networks. Phys. Rev. Lett. 107 (18), 180602.
Kang, P.K., Anna, P., Nunes, J.P., Bijeljic, B., Blunt, M.J., Juanes, R., 2014. Pore-scale intermittent velocity structure underpinning anomalous transport through 3-D porous media. Geophys. Res. Lett. 41 (17), 6184–6190.
Kesten, H., 1982. Proofs of Theorems 3.1 and 3.2, in Percolation Theory For Mathematicians, Edited. Springer, pp. 168–197.
Kurz, D.L., Secchi, E., Carrillo, F.J., Bourg, I.C., Stocker, R., Jimenez-Martinez, J., 2022. Competition between growth and shear stress drives intermittency in preferential flow paths in porous medium biofilms. Proc. Natl. Acad. Sci. 119 (30), e2122202119.
Le Borgne, T., Dentz, M., Carrera, J., 2008. Lagrangian statistical model for transport in highly heterogeneous velocity fields. Phys. Rev. Lett. 101 (9), 090601.
Lenormand, R., Zarcone, C., Sarr, A., 1983. Mechanisms of the displacement of one fluid by another in a network of capillary ducts. J. Fluid Mech. 135, 337–353.
Levy, M., Berkowitz, B., 2003. Measurement and analysis of non-Fickian dispersion in heterogeneous porous media. J. Contam. Hydrol. 64 (3–4), 203–226. https://doi.org/10.1016/s0169-7722(02)00204-8.
Li, L., Zhou, H., Gómez-Hernández, J.J., 2011. Transport upscaling using multi-rate mass transfer in three-dimensional highly heterogeneous porous media. Adv. Water Resour. 34 (4), 478–489.
Liao, K., Scheidegger, A., 1969. Branching-type models of flow through porous media, international association of scientific hydrology. Bulletin 14 (4), 137–143.
Menke, H., Reynolds, C., Andrew, M., Nunes, J.P., Bijeljic, B., Blunt, M., 2018. 4D multi-scale imaging of reactive flow in carbonates: assessing the impact of heterogeneity on dissolution regimes using streamlines at multiple length scales. Chem. Geol. 481, 27–37.
Moisy, F.. Computing a fractal dimension with Matlab: 1D, 2D and 3D Box-counting. https://www.mathworks.com/matlabcentral/fileexchange/13063-boxcount.
Morales-Casique, E., Neuman, S.P., Guadagnini, A., 2006a. Nonlocal and localized analyses of nonreactive solute transport in bounded randomly heterogeneous porous media: computational analysis. Adv. Water Resour. 29 (9), 1399–1418.
Morales-Casique, E., Neuman, S.P., Guadagnini, A., 2006b. Non-local and localized analyses of non-reactive solute transport in bounded randomly heterogeneous porous media: theoretical framework. Adv. Water Resour. 29 (8), 1238–1255.
Morales, V.L., Parlange, J.Y., Steenhuis, T.S., 2010. Are preferential flow paths perpetuated by microbial activity in the soil matrix? A review. J. Hydrol. 393 (1–2), 29–36 (Amst).
Moreno, L., Tsang, C.F., 1994. Flow channeling in strongly heterogeneous porous media: a numerical study. Water Resour. Res. 30 (5), 1421–1430.
Obi, I.S., Onuoha, K.M., Obilaja, O.T., Dim, C., 2020. Understanding reservoir heterogeneity using variography and data analysis: an example from coastal swamp deposits, Niger Delta Basin (Nigeria). Geologos 26.
Pereira Nunes, J., Blunt, M., Bijeljic, B., 2016. Pore-scale simulation of carbonate dissolution in micro-CT images. J. Geophys. Res. Solid Earth 121 (2), 558–576.
Pharoah, J., Karan, K., Sun, W., 2006. On effective transport coefficients in PEM fuel cell electrodes: anisotropy of the porous transport layers. J. Power Sources 161 (1), 214–224.
Raveh-Rubin, S., Edery, Y., Dror, I., Berkowitz, B., 2015. Nickel migration and retention dynamics in natural soil columns. Water Resour. Res. 51 (9), 7702–7722.
Riva, M., De Simoni, M., Willmann, M., 2005. Impact of the choice of the variogram model on flow and travel time predictors in radial flows. Geostatistics for Environmental Applications, Edited. Springer, pp. 273–284.
Riva, M., Guadagnini, L., Guadagnini, A., 2010. Effects of uncertainty of lithofacies, conductivity and porosity distributions on stochastic interpretations of a field scale tracer test. Stoch. Environ. Res. Risk Assess. 24 (7), 955–970.
Riva, M., Guadagnini, A., Fernandez-Garcia, D., Sanchez-Vila, X., Ptak, T., 2008. Relative importance of geostatistical and transport models in describing heavily tailed breakthrough curves at the Lauswiesen site. J. Contam. Hydrol. 101 (1–4), 1–13.
Riva, M., Guadagnini, A., Neuman, S.P., Janetti, E.B., Malama, B., 2009. Inverse analysis of stochastic moment equations for transient flow in randomly heterogeneous media. Adv. Water Resour. 32 (10), 1495–1507. https://doi.org/10.1016/j.advwatres.2009.07.003.
Rizzo, C.B., de Barros, F.P., 2017. Minimum hydraulic resistance and least resistance path in heterogeneous porous media. Water Resour. Res. 53 (10), 8596–8613.
Salamon, P., Fernàndez-Garcia, D., Gómez-Hernández, J., 2006a. Modeling mass transfer processes using random walk particle tracking. Water Resour. Res. 42 (11).
Salamon, P., Fernàndez-Garcia, D., Gómez-Hernández, J.J., 2006b. A review and numerical assessment of the random walk particle tracking method. J. Contam. Hydrol. 87 (3–4), 277–305.
Sánchez-Vila, X., Carrera, J., 2004. On the striking similarity between the moments of breakthrough curves for a heterogeneous medium and a homogeneous medium with a matrix diffusion term. J. Hydrol. 294 (1–3), 164–175 (Amst).
Sanchez-Vila, X., Guadagnini, A., Carrera, J., 2006. Representative hydraulic conductivities in saturated groundwater flow. Rev. Geophys. 44 (3).
Shao, W., Bogaard, T., Bakker, M., Greco, R., 2015. Quantification of the influence of preferential flow on slope stability using a numerical modelling approach. Hydrol. Earth Syst. Sci. 19 (5), 2197–2212.
Stauffer, D., Aharony, A., 2018. Introduction to Percolation Theory. CRC Press.
Torelli, L., Scheidegger, A.E., 1972. Three-dimensional branching-type models of flow through porous media. J. Hydrol. 15 (1), 23–35 (Amst).
Tufenkji, N., Elimelech, M., 2004. Correlation equation for predicting single-collector efficiency in physicochemical filtration in saturated porous media. Environ. Sci. Technol. 38 (2), 529–536.
Tyukhova, A.R., Kinzelbach, W., Willmann, M., 2015. Delineation of connectivity structures in 2-D heterogeneous hydraulic conductivity fields. Water Resour. Res. 51 (7), 5846–5854.
Webb, E.K., Anderson, M.P., 1996. Simulation of preferential flow in three-dimensional, heterogeneous conductivity fields with realistic internal architecture. Water Resour. Res. 32 (3), 533–545.
Willmann, M., Carrera, J., Sánchez-Vila, X., 2008. Transport upscaling in heterogeneous aquifers: what physical parameters control memory functions? Water Resour. Res. 44 (12).
Xia, Y., Cai, J., Wei, W., Hu, X., Wang, X., Ge, X., 2018. A new method for calculating fractal dimensions of porous media based on pore size distribution. Fractals 26 (01), 1850006.
Yang, K., Vafai, K., 2011a. Transient aspects of heat flux bifurcation in porous media: an exact solution. J. Heat Transf. 133 (5).
Yang, K., Vafai, K., 2011b. Analysis of heat flux bifurcation inside porous media incorporating inertial and dispersion effects–an exact solution. Int. J. Heat Mass Transf. 54 (25–26), 5286–5297.
Ye, Y., Chiogna, G., Cirpka, O.A., Grathwohl, P., Rolle, M., 2015. Enhancement of plume dilution in two-dimensional and three-dimensional porous media by flow focusing in high-permeability inclusions. Water Resour. Res. 51 (7), 5582–5602.
Yoon, H., Chojnicki, K.N., Martinez, M.J., 2019. Pore-scale analysis of calcium carbonate precipitation and dissolution kinetics in a microfluidic device. Environ. Sci. Technol. 53 (24), 14233–14242.
Yu, B., Cheng, P., 2002. A fractal permeability model for bi-dispersed porous media. Int. J. Heat Mass Transf. 45 (14), 2983–2993.
Yu, B., Liu, W., 2004. Fractal analysis of permeabilities for porous media. AIChE J. 50 (1), 46–57.

Zehe, E., Loritz, R., Edery, Y., Berkowitz, B., 2021. Preferential pathways for fluid and solutes in heterogeneous groundwater systems: self-organization, entropy, work. Hydrol. Earth Syst. Sci. Discuss. 1–28.
Zhang, X., Lv, M., 2007. Persistence of anomalous dispersion in uniform porous media demonstrated by pore-scale simulations. Water Resour. Res. 43 (7).
Zolezzi, G., Bertoldi, W., Tubino, M., Smith, G., Best, J., Bristow, C., Petts, G., 2006. Morphological analysis and prediction of river bifurcations, Braided rivers: process, deposits. Ecol. Manag. 36, 233–256.